An enhanced perturbational study on spectral properties of the Anderson model

1995 J. Phys.: Condens. Matter 7 2801

(http://iopscience.iop.org/0953-8984/7/14/018)

J. Phys.: Condens. Matter 7 (1995) 2801–2818. Printed in the UK

An enhanced perturbational study on spectral properties of the Anderson model

F B Anders

Institut für Festkörperphysik, Technische Hochschule D-64289 Darmstadt, Germany

Received 4 January 1995

Abstract. The infinite-U single-impurity Anderson model for rare earth alloys is examined with a new set of self-consistent coupled integral equations, which can be embedded in the large-N expansion scheme (N is the local spin degeneracy). The finite-temperature impurity density of states (DOS) and the spin-fluctuation spectra are calculated exactly up to the order $O(1/N^2)$. The presented conserving approximation goes well beyond the $1/N$ approximation (NCA) and maintains local Fermi-liquid properties down to very low temperatures. The position of the low-lying Abrikosov–Suhl resonance (ASR) in the impurity DOS is in accordance with Friedel's sum rule. For $N = 2$ its shift toward the chemical potential, compared to the NCA, can be traced back to the influence of the vertex corrections. The width and height of the ASR are governed by the universal low-temperature energy scale T_K. Temperature and degeneracy N dependence of the static magnetic susceptibility is found to be in excellent agreement with the Bethe *ansatz* results. Threshold exponents of the local propagators are discussed. The resonant level regime ($N = 1$) and intermediate-valence regime ($|\epsilon_f| < \Delta$) of the model are thoroughly investigated as a critical test of the quality of the approximation. Some applications to the Anderson lattice model are pointed out.

1. Introduction

Recently a major improvement has been reported on the perturbational approach to the single-impurity Anderson model (SIAM) with N-fold degenerate local state in the limit of infinitely large Coulomb repulsion U[3]. The aim of this paper is to present in detail the results obtained so far with this so-called post-NCA theory ($PNCA_\infty$). This approximation contains a resumation of infinite numbers of skeleton diagrams and is exact up to order $O(1/N^2)$. The skeleton diagrams included physically describe complicated multiexcitation processes.

The paper is organized as follows: in section 2, the large-N expansion is used to derive the self-consistent coupled integral equation for the self-energies and the vertex function. The physical processes included will be explained. In section 3 numerically obtained solutions for the local propagators will be presented and their threshold exponents related to results furnished by other methods. A detailed analysis of the one-particle spectra will be the topic of section 4 including a discussion of the Fermi-liquid properties and the impact of the vertex corrections. In section 5, we will develop a theory of the magnetic vertex correction exact up to $O(1/N^3)$ and compare the calculated static magnetic susceptibility with the Bethe *ansatz* results. Spin-fluctuation spectra will also be covered. The two critical cases, the intermediate-valence and the resonant level case, will be thoroughly examined in section 6. In section 7, a summary and an outlook on further applications will be given.

0953-8984/95/142801+18$19.50

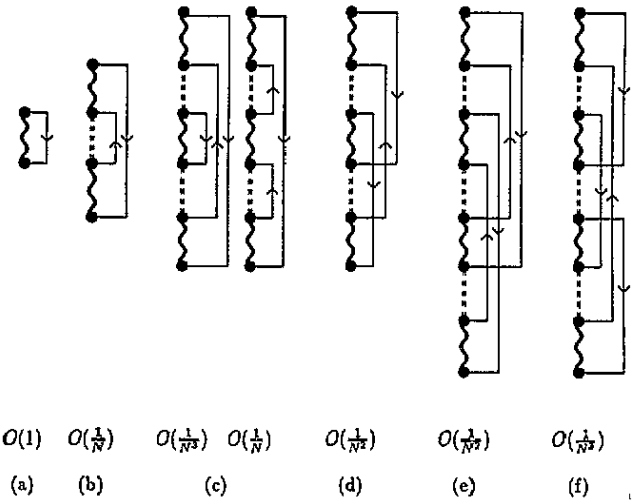

Figure 1. Diagrammatic contributions to the self-energy $\Sigma_0(z)$ of the unoccupied propagator P_0 up to V^8.

2. Theory

In direct perturbation theory a well established set of diagrammatical rules has been established to evaluate self-energy contributions to the local propagator $P_M(z)$ [12, 5]. In figure 1 the lowest-order contributions up to V^8 to the self-energy $\Sigma_0(z)$ of propagator $P_0(z)$ of the unoccupied state are shown. Contributions (b) and (c) are one-particle irreducible but contain self-energy insertions and are already included in the skeleton diagram (a). In order V^6 there exists only *one* skeleton diagram, whereas there are exactly *two* in order V^8. To include these higher-order corrections, a well established concept of vertex functions is used. In our case, a vertex function is defined by cutting the electron and the local propagator line at the uppermost vertex in each skeleton diagram and by summing up all contributions of the remaining lower parts of the skeletons. The concept of vertex function has already been successfully applied in an NCA theory (non-crossing approximation) for the finite-U Anderson model [16]. The resulting dimensionless factor $\Delta^{\mathrm{i}}_m(x, y)$ renormalizes the bare hybridization vertex V of an absorbed band electron in an energy-dependent way; x is the ingoing and y the outgoing energy of the local propagator. The corresponding vertex function $\Delta^{\mathrm{o}}_m(x, y)$ for an emitted band electron is obtained from the vertex function of an absorbed electron $\Delta^{\mathrm{i}}_m(x, y)$ by symmetry: $\Delta^{\mathrm{o}}_m(x, y) = \Delta^{\mathrm{i}}_m(y, x)$. Therefore we only calculate $\Delta_m(x, y) \equiv \Delta^{\mathrm{i}}_m(x, y)$. In a formal way all skeleton diagrams are summed up by using the exact vertex function in

$$\Sigma_0(z) = V^2 \sum_{km} f(\epsilon_k)\Delta_m(z, z + \epsilon_k)P_m(z + \epsilon_k) \tag{1}$$

$$\Sigma_m(z) = V^2 \sum_{k} f(-\epsilon_k)\Delta_m(z - \epsilon_k, z)P_m(z - \epsilon_k). \tag{2}$$

Approximations are made by the selection of contributions to Δ_m. The NCA, for example, is recovered by setting $\Delta_m(x, y) = 1$.

In order to derive the integral equation for the vertex function exactly up to $O(1/N^2)$ the lower parts of the skeleton diagrams (d) and (e) have to be included in addition to

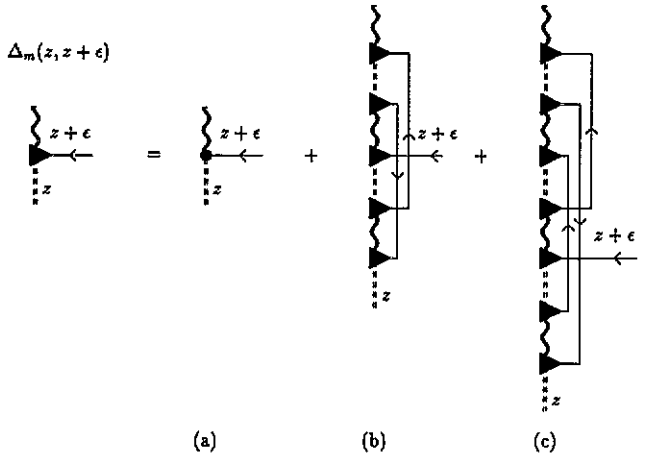

Figure 2. Diagrammatical representation of the self-consistency equation of the vertex function $\Delta_m(x, y)$ in $O(1/N^2)$.

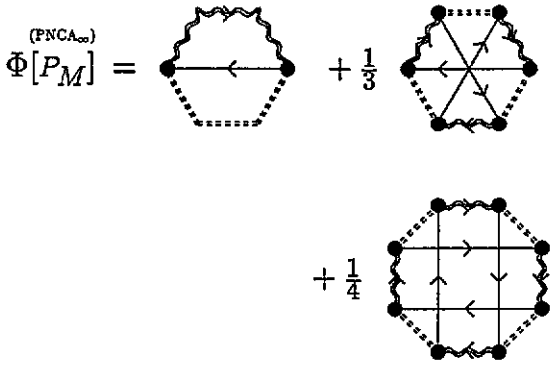

Figure 3. Generating functional for the self-energies and the Green's functions up to order $O(1/N^2)$. The PNCA_∞ contains additional higher-order contributions.

skeleton diagram (a). Skeleton (f) can be neglected, since it is of the order $O(1/N^3)$. The corresponding generating functional is shown diagrammatically in figure 3. An infinite number of skeletons are resummed by replacing the bare hybridization vertex by the renormalized one $V\Delta_m(x, y)$ in each diagram in order to include as many higher-order terms as possible. This yields a self-consistent equation for the vertex function displayed in figure 2 [3]. In the case of zero magnetic field all P_m are equal, and the vertex function

is reduced to

$$\Delta(x, y) \equiv \Delta_m(x, y)$$
$$= 1 - |V|^4 \int_{-\infty}^{\infty}\int_{-\infty}^{\infty} du\, dv\, \rho(u)\rho(v) f(u) f(-v) G(x, x+u, x+u-v)$$
$$\times \Delta(x+u-v, y+u-v) H(y, y-v, y+u-v). \tag{3}$$

Here we have chosen $\rho(\epsilon)$ to be the density of states (DOS) of the conduction electrons and the auxiliary functions G, H and K

$$G(x, x+u, x+u-v) = \Delta(x, x+u) P_m(x+u)$$
$$\times \Delta(x+u-v, x+u) P_0(x+u-v) \tag{4}$$

$$H(y, y-u, y+u-v) = P_m(y+u-v)(\Delta(y-v, y+u-v) P_0(y-v) \Delta(y-v, y)$$
$$- K(y+u-v, y, y+u)) \tag{5}$$

$$K(y+u-v, y, y+u) = N|V|^2 \int_{-\infty}^{\infty} dl\, \rho(l) f(-l) \Delta(y+u-v-l, y+u-v)$$
$$\times P_0(y+u-v-l) \Delta(y+u-v-l, y+u-l)$$
$$\times P_m(y+u-l) \Delta(y-l, y+u-l)$$
$$\times P_0(y-l) \Delta(y-l, y). \tag{6}$$

The negative sign in equation (3) takes into account the odd number of crossing electron lines in the skeleton (d) while in diagram (e) an even number of crossing lines can be found. The approximation defined by equations (1) to (6) will be called PNCA_∞ in the following (∞ stands for $U = \infty$).

In the one-particle Green's function $F_m(i\omega_n)$ the vertex correction also comes into play in a natural way [7]:

$$F_m(i\omega_n) = \frac{1}{Z_f} \oint_C \frac{dz}{2\pi i} e^{-\beta z} \Delta_m(z, z+i\omega_n) P_0(z) P_m(z+i\omega_n). \tag{7}$$

This equation can e.g. be obtained by cutting one band electron line in the functional $\Phi[P_M]$ of figure 3. Thereby, no ambiguity is left in the analytic expression. The contour C encircles all the singularities of the kernel in an anticlockwise fashion. Analytic continuation of the Green's function gives

$$F_m(\omega + i\delta) = \int_{-\infty}^{\infty} dw'\, P_m(\omega + w')(\Re\Delta_x(\omega, \omega+w')\xi_0(w')$$
$$+ \Re e[P_0(w')]\xi_{\Delta_x}(\omega, \omega+w'))$$
$$- \int_{-\infty}^{\infty} dw'\, P_0^*(w'-\omega)(\Re\Delta_y(w'-\omega, \omega)\xi_m(w')$$
$$+ \Re e[P_m(w')]\xi_{\Delta_y}(w'-\omega, w')). \tag{8}$$

We have introduced the real auxiliary functions

$$\xi_M(\omega) \equiv -\frac{1}{\pi Z_f} e^{-\beta\omega}\, \Im m P_M(\omega + i\delta) \tag{9}$$

and the complex auxiliary functions

$$\begin{aligned}
\Re\Delta_x(\omega,\omega+\mathrm{i}\omega_n) &\equiv \tfrac{1}{2}[\Delta(\omega+\mathrm{i}\delta,\omega+\mathrm{i}\omega_n) + \Delta(\omega-\mathrm{i}\delta,\omega+\mathrm{i}\omega_n)]\\
\Im\Delta_x(\omega,\omega+\mathrm{i}\omega_n) &\equiv (1/2\mathrm{i})[\Delta(\omega+\mathrm{i}\delta,\omega+\mathrm{i}\omega_n) - \Delta(\omega-\mathrm{i}\delta,\omega+\mathrm{i}\omega_n)]\\
\Re\Delta_y(\omega-\mathrm{i}\omega_n,\omega) &\equiv \tfrac{1}{2}[\Delta(\omega-\mathrm{i}\omega_n,\omega+\mathrm{i}\delta) + \Delta(\omega-\mathrm{i}\omega_n,\omega-\mathrm{i}\delta)]\\
\Im\Delta_y(\omega-\mathrm{i}\omega_n,\omega) &\equiv (1/2\mathrm{i})[\Delta(\omega-\mathrm{i}\omega_n,\omega+\mathrm{i}\delta) - \Delta(\omega-\mathrm{i}\omega_n,\omega-\mathrm{i}\delta)]\\
\xi_{\Delta_x}(x,y) &\equiv -(1/\pi Z_\mathrm{f})\mathrm{e}^{-\beta x}\,\Im\Delta_x(x,y)\\
\xi_{\Delta_y}(x,y) &\equiv -(1/\pi Z_\mathrm{f})\mathrm{e}^{-\beta y}\,\Im\Delta_y(x,y).
\end{aligned} \tag{10}$$

The functions $\xi_M(\omega)$ introduced above have a simple physical meaning as *defect propagator*: integration over the whole frequency range yields the occupation probability $\langle \hat{X}_{MM}\rangle$ of the local state M. The complex functions $\Re\,(\Im)\,\Delta_{x(y)}$ and $\xi_{\Delta_{x,y}}(x,y)$ enable the evaluation of equation (7) for real frequencies and thus serve purely numerical purposes.

3. Local propagators, threshold exponents and specific heat

On a cluster of workstations, we brought a numerical iteration procedure for the above system of integral equations to full convergence using dynamically defined logarithmic meshes for the threefold integration in (3). Besides the modulus $||P_M^{(i)} - P_M^{(i+1)}||$ (i labels the step of iteration), which reaches a value of typically 10^{-16} at the end, the sum rules

$$\begin{aligned}
&\oint_C \frac{\mathrm{d}z}{2\pi\mathrm{i}} P_M(z) = 1\\
&\oint_C \frac{\mathrm{d}z}{2\pi\mathrm{i}} \Sigma_M(z) = |V|^2 \sum_{km} \left(\langle M|\hat{n}_m^\mathrm{f}|M\rangle[1-f(\epsilon_{km})] + \langle M|(1-\hat{n}_m^\mathrm{f})|M\rangle f(\epsilon_{km})\right)
\end{aligned} \tag{11}$$

have been checked to estimate the quality of the numerical calculations. The deviation between left and right side is in the range of typically 1–4% and scales with the inverse number of mesh points. For all numerical studies all energies are measured in units of the Anderson width $\Delta = \pi V^2 \mathcal{N}_\mathcal{F}$ (V^2 is the square of the hybridization matrix element and $\mathcal{N}_\mathcal{F}$ the band DOS at the chemical potential). The featureless symmetric conduction band DOS has been chosen to be $\rho^\mathrm{c}(\omega) = [1/2\Gamma(1.25)W]\exp(-(\omega/W)^4)$ to reduce band edge effects. The half band width is set to $W = 10\Delta$. In most cases the temperature will be measured in units of the corresponding Kondo energy

$$T_\mathrm{K} = W\left(\frac{\Delta}{\pi W}\right)^{1/N} \exp\left(-\frac{\pi|\epsilon_\mathrm{f}|}{N\Delta}\right). \tag{12}$$

For the investigation of the Kondo regime $\epsilon_\mathrm{f} = -3\Delta$ and $N = 2$ is chosen, since the largest impact of the vertex function is to be expected for small N. In figure 4 the spectral density $\rho_0(\omega) \equiv (1/\pi)\Im\mathrm{m}P_0(\omega - \mathrm{i}\delta)$ is displayed in the vicinity of the threshold for three different temperatures $T = 0.5,\ 1,\ 2T_\mathrm{K}$. Note the fact that the energy scale has been shifted by the threshold energy E_s. The transformation

$$Z_\mathrm{f} = \oint \frac{\mathrm{d}z}{2\pi\mathrm{i}} \mathrm{e}^{-\beta z} P_M(z) \equiv \mathrm{e}^{-\beta E_\mathrm{s}} \tilde{Z}_\mathrm{f}$$

defining a renormalized local partition function

$$\tilde{Z}_\mathrm{f} = \oint \frac{\mathrm{d}z}{2\pi\mathrm{i}} \mathrm{e}^{-\beta z} \tilde{P}_M(z)$$

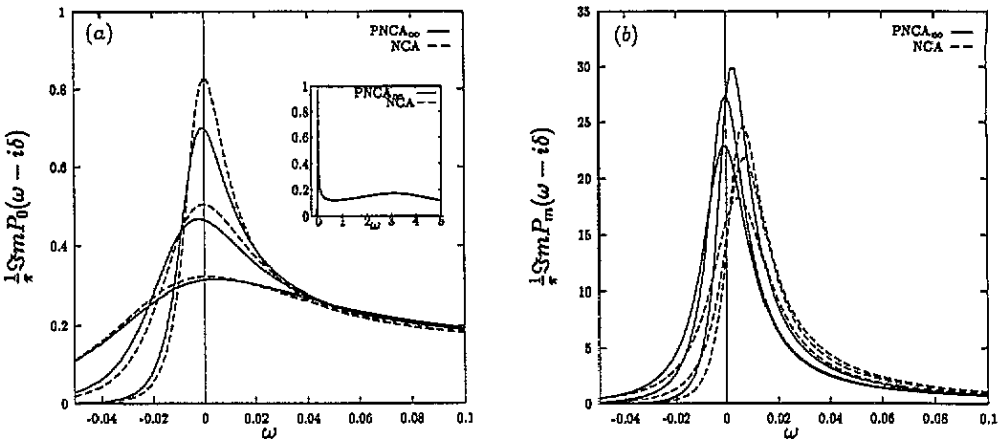

Figure 4. Comparison of the spectra of $P_0(\omega)$ (a) and $P_m(\omega)$ (b) in NCA and PNCA$_\infty$ at $T = 0.5, 1.0, 2.0T_K$. The increase in height at $\omega = 0$ is correlated with a decrease of temperature. Parameters: $N = 2, \epsilon_f = -3\Delta, W = 10\Delta$.

and a local propagator $\tilde{P}_M(z) \equiv P_M(z + E_s)$, ensures that the numerically calculated $\tilde{Z}_f$ stays of the order O(1) during the variation of temperature. Also the *defect propagators* ξ_M can be calculated very accurately down to very low temperatures.

With decreasing temperature the threshold behaviour of the propagator P_0 in PNCA$_\infty$ exhibits a weaker increase than the corresponding NCA propagator. We regard this as a strong hint toward a reduced threshold exponent α_0 compared with the NCA due to the influence of the vertex corrections. On the other hand, the inset of figure 4(a) indicates quite clearly an excellent agreement on the high-energy part of the spectrum in both approximations as to be expected. The spectral density $\rho_m(\omega)$, shown in figure 4(b) for the same set of model parameters and temperatures, reveals an additional difference between the two approximations. P_0^{PNCA} and P_m^{PNCA} already develop their common threshold energy E_s at finite temperature while in NCA an identical E_s for both propagators is found only at $T = 0$. This gives rise to a temperature dependent position of the ASR in the one-particle spectra in NCA, as we will see in the next section.

To obtain a first estimate for threshold exponents we fit the ionic spectrum in the low-frequency range $0 < \omega < T_K$ to a trial function $h_M(\omega) = a(T)\omega^{-\alpha_M(T)}$ at different temperatures. This procedure has been checked for the NCA and provides the *exactly* known NCA exponents $\alpha_0 = N/(N+1)$ and $\alpha_m = 1/(N+1)$ within an accuracy of 5%. While no temperature dependence is found for the exponent $\alpha_0 = 0.44 \pm 0.02$, figure 5(a), the different values of $\alpha_m(T)$ have been used to to extrapolate $\alpha_m(0) = 0.27 \pm 0.01$ for the present parameters $N = 2, \epsilon_f = -3\Delta$ giving $n_f = 0.87$, figure 5(b).

There is still no agreement in the literature about the exact exponents for $N \geqslant 2$. The proposal of Menge and Müller-Hartmann [13]

$$\alpha_0 = \frac{n_f^2}{N} \qquad \alpha_m = \frac{n_f}{N}(2 - n_f) \tag{13}$$

indicates a dependence of the exponents not only on the degeneracy N but also on the occupation number n_f in all regimes. This proposal has been recently backed by a analysis of pseudo-boson and fermion propagators provided by the numerical renormalization group for $N = 2$ [6]. On the other hand, an analysis of parquet equations for the Kondo limit of

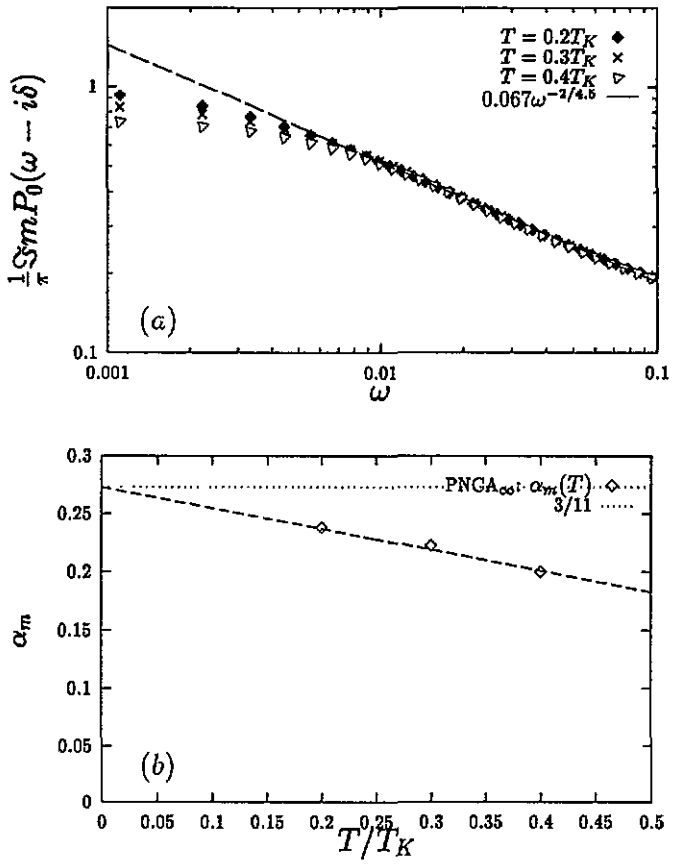

Figure 5. Threshold behaviour of the spectrum of $P_0(z)$ (a) and an estimation for the threshold exponent α_m (b). Parameters as before.

the model ($n_f = 1$) claims that the exponents

$$\alpha_0 = \frac{N - 2/N^2}{N + 1 - 2/N^2} \qquad \alpha_m = \frac{1 - 1/N^2}{N + 1 - 2/N^2} \tag{14}$$

should be exact to order $O(1/N^2)$ [11]. We did not investigate the threshold behaviour on the full scale of the model parameters. Therefore we cannot rule out any of the proposals, even though the PNCA$_\infty$ exponents in the Kondo regime come very close to Gruneberg's and Keiter's results.

Since we have convinced ourselves that the high-energy parts of the spectra remain unchanged, we can still use the NCA to obtain specific heat data for a wide temperature range. On the other hand, the low-energy corrections turn out to be essential for the calculation of correlation functions. In figures 6 and 7 origin and scaling behaviour of the two different contributions to the specific heat are clearly demonstrated. In (a) the effective hybridization is tuned leading to a renormalized Anderson width Δ^* and in (b) the position of the bare f-electron level has been varied for $N = 2$. While the first maximum in each curve of the specific heat turns out to be an universal function of T/T_K, the position of the second is rather determined by the f-level energy and its width by Δ^*. Therefore, the first peak is generated by spin excitations on the Kondo scale $T \sim T_K$, whereas the

second contains charge excitations from the broadened f-level into unoccupied band states. With increasing degeneracy the maximum due to spin excitations is enhanced essentially linearly with N [4], since their contribution is proportional to the number of channels, as is already known from Bethe *ansatz* calculations [17]. The charge excitation peak is rather decreased and smeared out by broadening of the f-level proportional to $N\Delta$. Its position and broadening is in good agreement with Bethe *ansatz* [14] and numerical renormalization group calculations [15], but the height comes out somewhat smaller. This could be due to the absence of the doubly occupied state for $U = \infty$. Of course, the appearance of the charge excitations is more of academic interest for the low-temperature behaviour, but may be important for spectroscopic studies.

4. One-particle spectra

The generalized Friedel's sum rule

$$n_f(T) = \frac{1}{\pi}\sum_m \int_{-\infty}^{\infty} d\omega\, (\partial_\omega f(\omega))\, \delta_m(\omega) + \underbrace{\frac{1}{2\pi i}\sum_m \oint_C dz\, f(z) F_m(z) \partial_z \Sigma_m(z)}_{\equiv \kappa(T)} \tag{15}$$

relates the local occupation number n_f to the generalized phase shifts $\delta_m(\omega) \equiv -\Im m \ln\left[-F_m^{-1}(i\delta)\right]$. κ essentially measures the asymmetry of the f-electron spectrum and can be interpreted as the negative change of the number of band electrons in the presence of the impurity [1]. In the limit $T = 0$, equation (15) is used in combination with local Fermi-liquid relations to derive the density of states rule:

$$\rho^{(f)}(0, T = 0) = \frac{1}{\pi\Delta}\sin^2\left(\frac{\pi(n_f - \kappa)}{N}\right). \tag{16}$$

This formula predicts a scattering resonance with a maximum height of $1/\pi\Delta$ near the chemical potential ($(n_f - \kappa) \approx 1$) for $N = 2$ and $T = 0$, the ASR, which moves away from μ with increasing degeneracy N. Figure 8 shows the one-particle spectra of PNCA$_\infty$ and NCA for five values of temperature. The most significant differences between both approximations concern the position and height of the ASR. The position in NCA is found to be strongly temperature dependent and the height already exceeds the unitarity limit of $1/(\pi\Delta)$ at temperatures slightly below T_K. We can trace back the temperature dependence to the mismatch of the threshold energies of P_0 and P_m, which merge only at $T = 0$. The violation of equation (16) clearly indicates the importance of the vertex corrections. On the other hand, the PNCA$_\infty$ ASR grows with decreasing temperature at a stable position close to the chemical potential. It violates only sightly the density of states sum rule and its agreement with Friedel's sum rule (15) is found to be within 7% as indicated in table 1.

By focusing our attention on figure 9, we gain insight on the impact of vertex corrections on the the ASR. The PNCA$_\infty$ result (solid curve) is compared to the NCA result (dashed curve) for the fixed temperature $T = 0.5T_K$ and additionally to a curve where the NCA propagators $P_M(z)$ have been used to evaluate the renormalized hybridization $V\Delta(x, y)$ via equation (3). In the later convergence is achieved after two steps of iteration. The resulting ASR, calculated after each step, has been shifted towards the chemical potential, but stays enhanced compared to the PNCA$_\infty$ ASR. The reduction of height of the ASR is clearly connected to the modified threshold exponents as is also revealed by an inspection of the iteration procedure. This stressed the importance of vertex corrections in the local propagators $P_M(z)$.

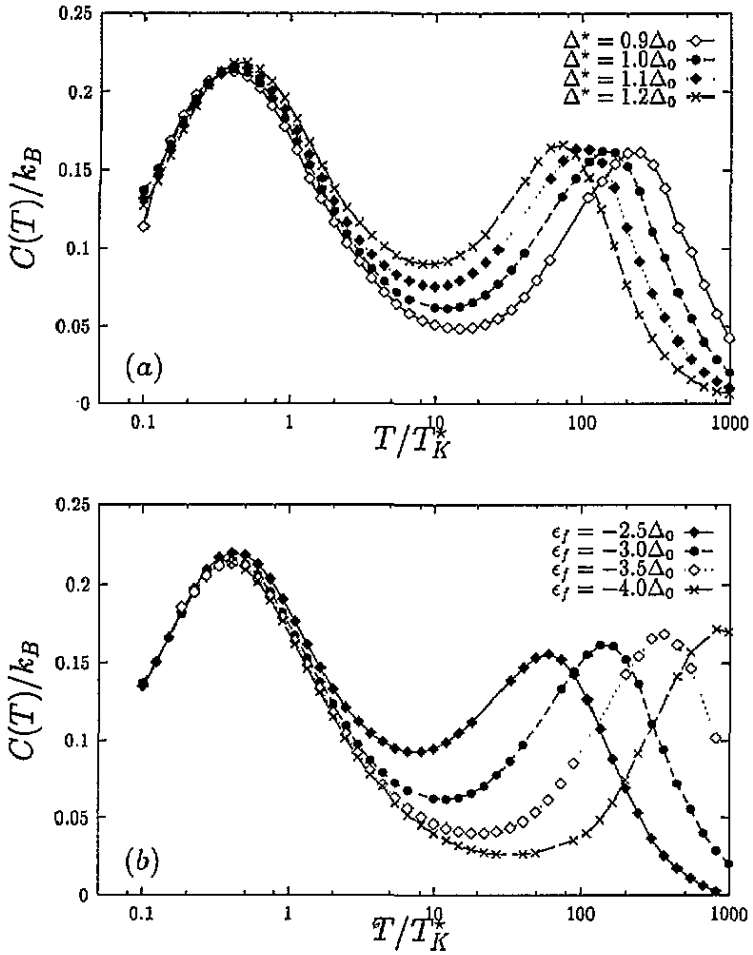

Figure 6. Specific heat contribution of the impurity versus temperature T/T_K for (a) different values of the effective Anderson width $\Delta^* = \pi|V^*|^2\rho_0$, $\epsilon_f = -3\Delta_0$, and (b) different values of ϵ_f. Parameters: $N = 2$, $\epsilon_f = -3\Delta_0$, $\Delta_0 = 0.1W$.

The plots in figure 10 attract attention to the local Fermi-liquid properties as seen in the imaginary part of the self-energy of the Green's function:

$$\Im\mathrm{m}\Sigma_{fm}(\omega - \mathrm{i}\delta) = \Delta + C_\omega\omega^2 + C_T T^2. \tag{17}$$

From the symmetric Anderson model it is known that $C_\omega = \Delta/T_K^2$ and $C_T = \Delta(\pi^2/T_K^2)$ [10]. In the strongly asymmetric case ($U = \infty$) under consideration here, only the scaling $C_\omega = \Delta/T_K^2$ can be found. The quadratic expansion coefficient for the temperature exhibits a rather strong dependence on the degeneracy N as been shown in figure 10, originating from the shift of the ASR away from the chemical potential, while in the completely symmetric case the phase shift δ_m remains $\pi/2$ independently of N. On the base of our PNCA$_\infty$ results we suggest a new analytic investigation of Fermi-liquid relations for the asymmetric case.

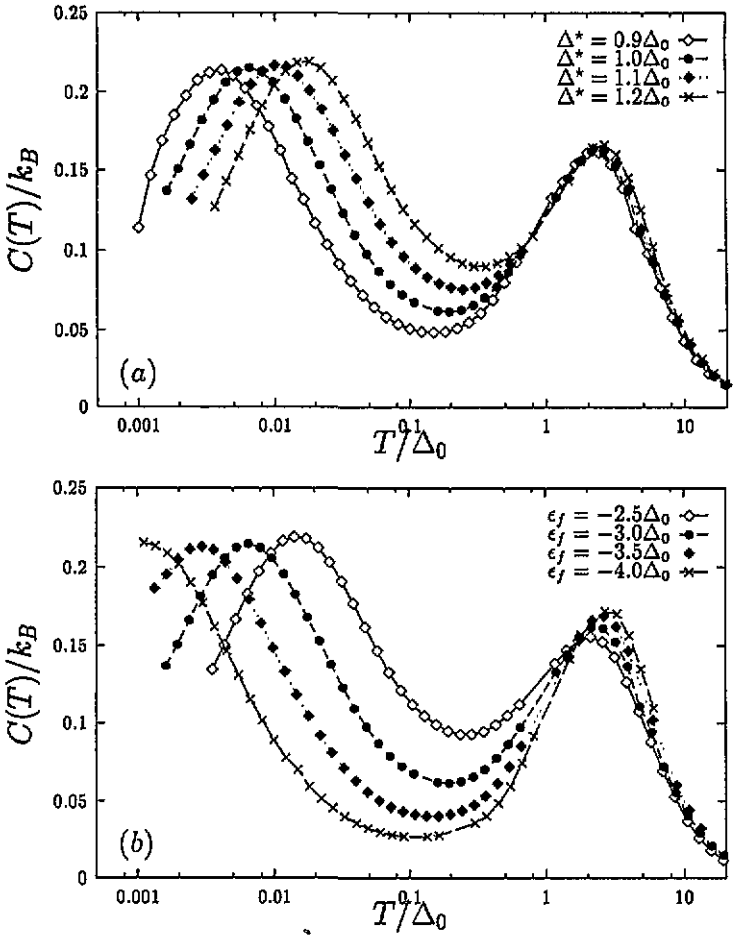

Figure 7. Specific heat contribution of the impurity versus temperature T/Δ_0 for (a) different values of the effective Anderson width $\Delta^* = \pi|V^*|^2\rho_0$, $\epsilon_f = -3\Delta_0$, and (b) different values of ϵ_f. Parameters: $N = 2$, $\epsilon_f = -3\Delta_0$, $\Delta_0 = 0.1W$.

5. Magnetic susceptibility and spin fluctuations

Magnetic excitations are measured by the magnetic susceptibility:

$$\chi(\mathrm{i}\nu_n) = -\frac{1}{Z}\oint_C \frac{\mathrm{d}z}{2\pi\mathrm{i}} \mathrm{e}^{-\beta z}\,\mathrm{Tr}\left[\frac{1}{z-\hat{H}}\hat{M}\frac{1}{z+\mathrm{i}\nu_n-\hat{H}}\hat{M}\right] = \chi(-\mathrm{i}\nu_n) \qquad (18)$$

where $\mathrm{i}\nu_n = 2\pi\mathrm{i}n/\beta$ is a bosonic Matsubara frequency. Focusing our attention on the operator for the local magnetization in the SIAM, $\hat{M}_z \equiv g\mu_B \sum_m m\,\hat{X}_{m,m}$, we rewrite $\chi_f(\mathrm{i}\nu_n)$ in analogy to F_m:

$$\chi_f(\mathrm{i}\nu_n) = -\frac{N\mu_j^2}{3}\frac{1}{Z_f}\oint_C \frac{\mathrm{d}z}{2\pi\mathrm{i}} \mathrm{e}^{-\beta z} P_m(z) P_m(z+\mathrm{i}\nu_n)\Gamma(z, z+\mathrm{i}\nu_n) \qquad (19)$$

defining $\mu_j^2 \equiv j(j+1)(g\mu_B)^2$. The new magnetic vertex function $\Gamma(x, y)$ formally includes all higher-order contributions arising from diagrams with crossing band electron lines; in NCA $\Gamma(x, y) = 1$. It turns out to be symmetric in its complex energy arguments in order to maintain the symmetry $\chi(\mathrm{i}\nu_n) = \chi(-\mathrm{i}\nu_n)$. Using the standard set of diagrammatical

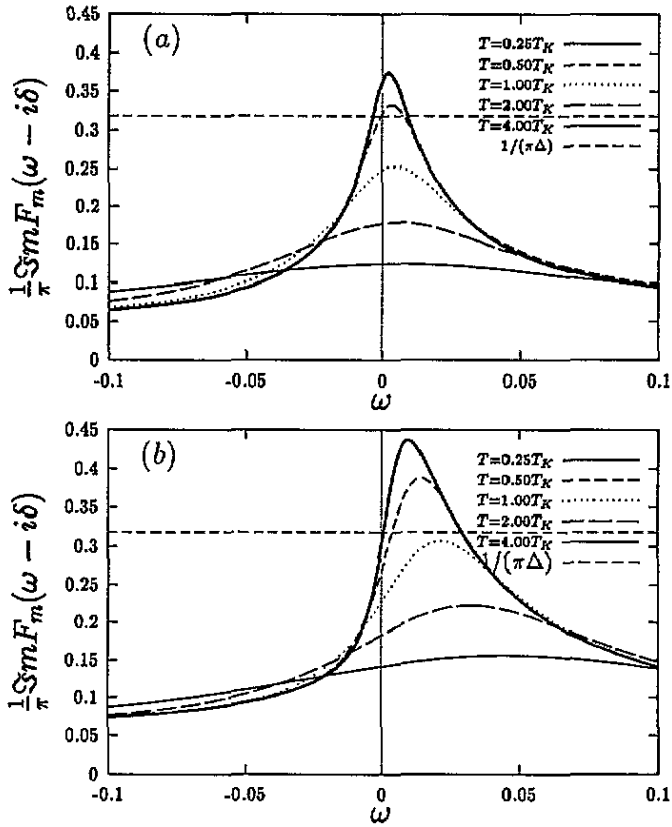

Figure 8. Temperature dependence of the ASR (a) in PNCA_∞ and (b) in NCA. Parameters: as before.

Table 1. Parameters: $N = 2$, $\epsilon_f = -3\Delta$, $W = 10$.

(a) Friedel's sum rule and the NCA theory			
T/T_K	n_f	$\sum_m \frac{\delta_m}{\pi}$	κ_{res}
0.1	0.8682	0.5863	0.2819
0.2	0.8682	0.6114	0.2567
0.3	0.8682	0.6379	0.2303
(b) Friedel's sum rule and the PNCA_∞ theory			
T/T_K	n_f	$\sum_m \frac{\delta_m}{\pi}$	κ_{res}
0.1	0.8445	0.9023	−0.0577
0.2	0.8525	0.9140	−0.0615
0.3	0.8565	0.9207	−0.0641

rules [5], we obtain $\Gamma(x, y)$ exactly up to order $O(1/N^3)$ shown in figure 11. $O(1/N^2)$ contributions compensate each other. On the other hand, diagrams (b) and (c) in figure 11 transform into each other by exchanging the energy arguments. Therefore, we only have to

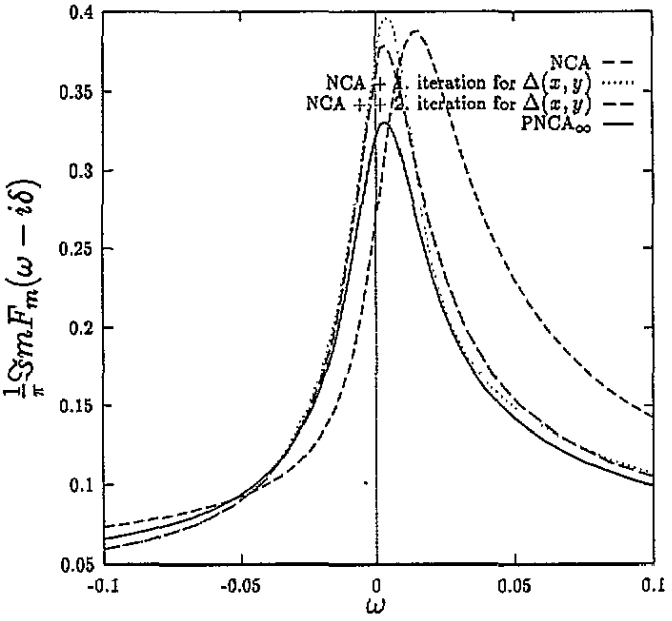

Figure 9. Impact of the vertex correction on the one-particle spectrum. Parameters: as before.

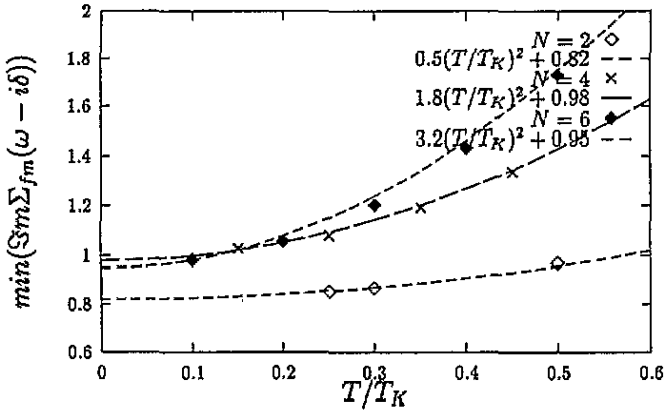

Figure 10. *Minimum of the self-energy versus temperature for* $N = 2, 4, 6$. *Parameters:* $\epsilon_f(N=2) = -3\Delta$, $\epsilon_f(N=4) = -5\Delta$, $\epsilon_f(N=6) = -6.7\Delta$, $W = 10\Delta$.

insert

$$\begin{aligned}\Gamma_b(x,y) = -|V|^4 \int_{-\infty}^{\infty}\int_{-\infty}^{\infty} du\, dv\, \rho(u)\rho(v) f(-l) f(-u) f(v) \\ \times P_0(x-u)\Delta(x-u,x) \\ \times P_m(x-u+v)\Delta(x-u, x-u+v) \\ \times \Gamma(x-u+v, y-u+v) \\ \times P_m(y-u+v) j(y+u-v, y, y+u)\end{aligned} \tag{20}$$

into the magnetic vertex function of the $PNCA_\infty$ theory

$$\Gamma(x,y) = 1 + \Gamma_b(x,y) + \Gamma_b(y,x) \tag{21}$$

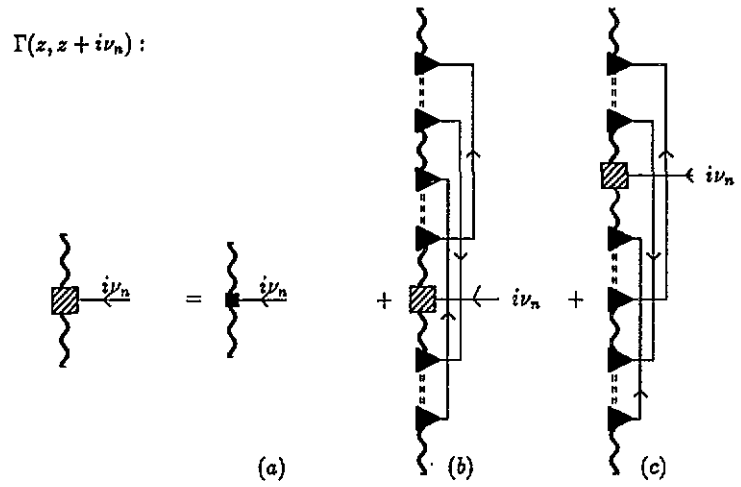

Figure 11. Diagrammatic representation of the self-consistency condition of the magnetic vertex function $\Gamma(x, y)$.

and to solve equations (20) and (21) self-consistently. Equation (19) then leads to a local dynamical susceptibility χ_f, which is exact in $O(1/N^2)$.

The quality of the approximation has been checked by comparison of the static magnetic susceptibility $\chi_f(T) \equiv \lim_{\nu\to 0} \chi(\nu)$ to the *exact* Bethe *ansatz* results [17], figure 12. The PNCA_∞ susceptibility shows a surprisingly good agreement with the exact results, even though the Bethe *ansatz* susceptibility has been obtained for the Coqblin–Schrieffer model. In particular, the characteristic maximum for degeneracies $N \geqslant 3$ has been reproduced in PNCA_∞. On the other hand in NCA not even a saturation of χ_f occurs for $0.1T_K < T < T_K$ and $N = 2$. The deficiencies of the NCA do not show up so strongly at e.g. $N = 6$ or at higher temperatures $T > T_K$, where vertex corrections become less important.

The scattering function $S(\nu)$ for neutron scattering experiments is linked to the magnetic susceptibility by the dissipation-fluctuation theorem:

$$S(\omega) \sim \frac{1}{1 - \exp(-\beta\omega)} \Im\mathrm{m}\chi(\omega). \tag{22}$$

The right-hand side approaches the spin-fluctuation spectrum $\sigma(\omega) \equiv \Im\mathrm{m}\,\chi(\omega)/\omega$ for small ω. In figure 13 the spin-fluctuation spectra of the PNCA_∞ and the NCA are compared for three different degeneracies N at a fixed temperature $T = 0.2T_K$. The pronounced maxima of $\sigma^{\text{PNCA}}(\omega)$ for $N > 3$ resemble the maxima in the static susceptibility discussed before. They appear on the same energy scale $\omega(T) \approx 0.5T_K$. It is also interesting to note that even though no maximum is found for $N = 2$ a rather broad inelastic peak can be reported in $\sigma^{\text{PNCA}}(\omega)$ which is not seen in the NCA spectrum. Of course, this features disappears well above T_K for both approximations leaving a single elastic peak at $\omega = 0$ in the spectra. The low-frequency behaviour of $\Im\mathrm{m}\,\chi(\omega)$ can be interpolated by $\omega/(\Gamma_{\text{neut}}^2 + \omega^2)$. Γ_{neut} is the neutron scattering linewidth which is experimentally defined by the position of the maximum. Here, it is convenient to use

$$\frac{1}{\Gamma_{\text{neut}}^2} = \lim_{\omega\to 0} \frac{\Im\mathrm{m}\,\chi(\omega)}{\omega}. \tag{23}$$

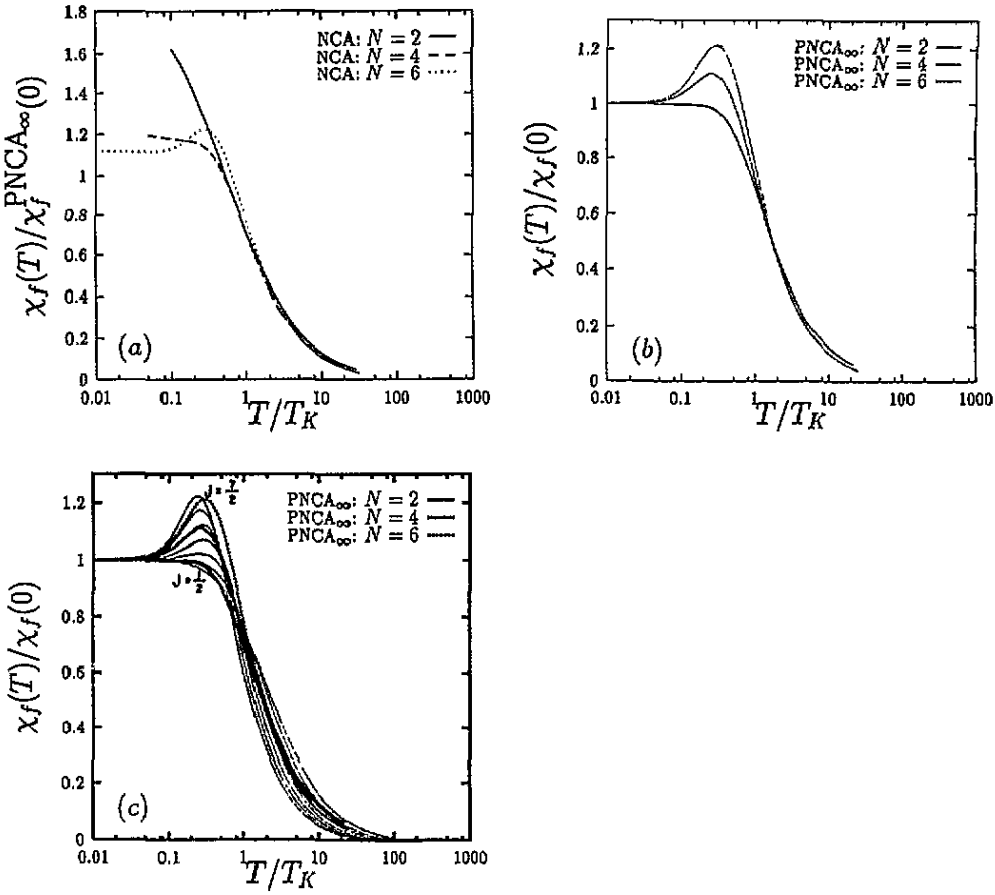

Figure 12. Static magnetic susceptibility calculated (a) in NCA, (b) in PNCA$_\infty$ for the single-impurity Anderson model and (c) for the Coqblin–Schrieffer models using the Bethe *ansatz* [17]. The NCA results are normalized with respect to the PNCA$_\infty$ values at $T = 0$. Parameters: as in figure 10.

In figure 14, the reduced linewidth $\Gamma_{\mathrm{neut}}/T_K$ is displayed versus temperature for $N = 2, 4, 6$ in PNCA$_\infty$. The linewidth is nearly temperature independent in the local Fermi-liquid regime at $T < T_K$. It develops a weak minimum at $T \approx 0.5T_K$ which is slightly enhanced by increasing degeneracy and behaves like $\sqrt{T}$ for high temperatures.

6. Critical examination of the PNCA$_\infty$

In the last three sections we discussed PNCA$_\infty$ results obtained for the Kondo regime of the model. In this section we will focus our attention on the case $N = 1$ and the mixed-valence regime. For $N = 1$ all diagrams are of the same order in the sense of an $1/N$ expansion scheme. Nevertheless, this classification is questionable here, since there is *no* Kondo effect left although the diagram topology remains unchanged. The one-particle Green's function is exactly known:

$$F(z) = \left(z - \epsilon_f - \frac{V^2}{\#k} \sum_k \frac{1}{z - \epsilon_k} \right)^{-1} \tag{24}$$

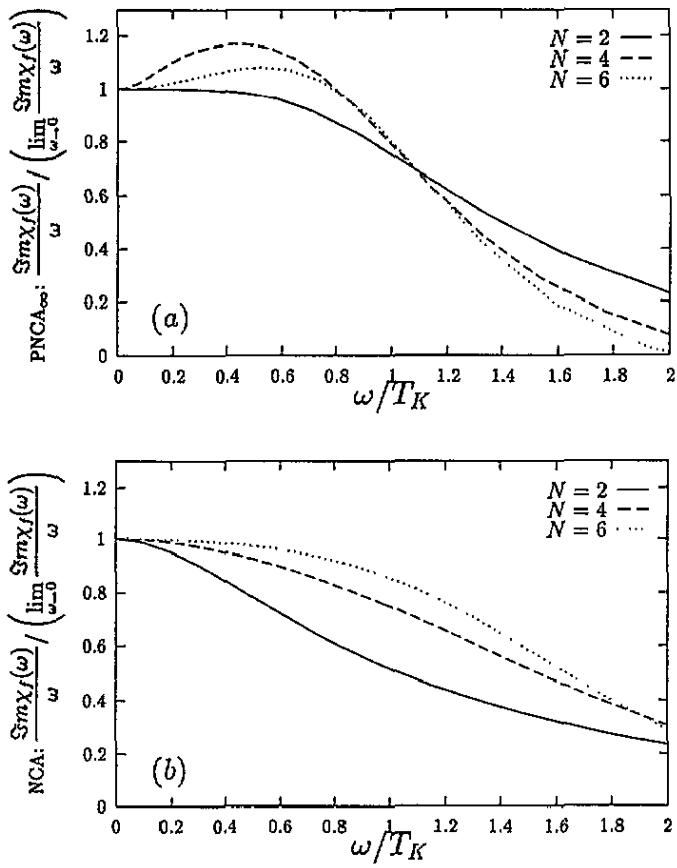

Figure 13. $\Im m\,\chi(\omega)/\omega$ versus ω/T_K for $N = 2, 4, 6$, calculated at $T = 0.2T_K$ (a) in PNCA$_\infty$ and (b) in NCA. Parameters: as in figure 10.

(#k denotes the number of band electron states). In figure 15 the one-particle spectra of the NCA and the PNCA$_\infty$ are compared with the exact result for two values of ϵ_f. While the $P_M(z)$ have been determined very accurately, oscillations of the defect propagators $\xi(\omega) = \exp(-\beta\omega)(1/\pi Z_f)\Im m\, P_M(\omega)$ during the iteration procedure cause oscillations in the PNCA$_\infty$ spectra around the exact solution, i.e. convergence is not fully obtained in this case. These oscillations contribute about 3% to the residual deviations of the PNCA$_\infty$. In the most critical case, $\epsilon_f = -\Delta$, the NCA is strongly pathological near μ, but the PNCA$_\infty$ is much less so. For $\epsilon_f = -3\Delta$ only a very weak pathology at $\mu = 0$ remains, while the NCA still produces an unphysical resonance at the chemical potential.

A rather strange two-peak structure is found in the spectrum for the case of the intermediate-valence regime $\epsilon_f = -\Delta$ and $N = 2$, shown in figure 16(a): the first peak nearly at $\mu = 0$ exceeds clearly the density of states rule (16) $\rho(0) = 0.21$ for $n_f \approx 0.6$, which would be the height of the minimum in between both peaks. We suppose that the *true* spectrum will monotonically decrease from the minimum position onwards for decreasing energy. The first peak clearly reflects a PNCA$_\infty$ pathology already seen in figure 15(a). Despite this spurious structure, the overall violation of the the DOS sum rule is reduced from almost 60% in NCA down to 15% in PNCA$_\infty$. In part (b) of the figure, ϵ_f is chosen to be $+\Delta$. Again, only a weak pathology is found in this case, and the spectrum can be

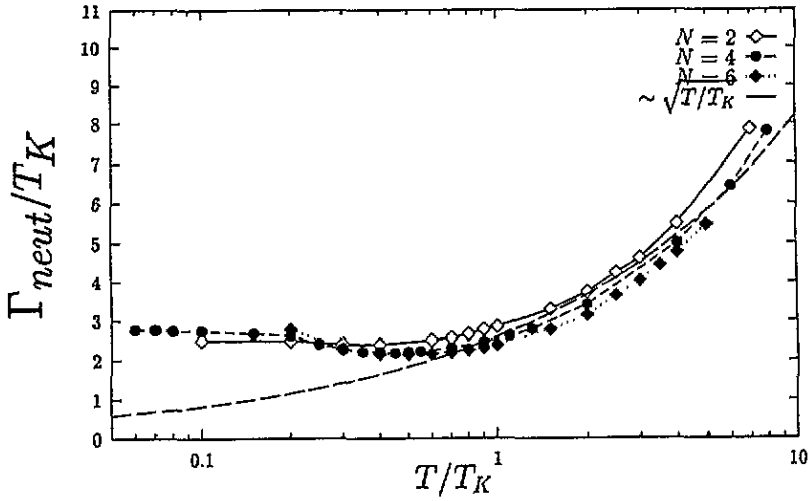

Figure 14. Neutron scattering linewidth Γ_{neut} versus T/T_K calculated in PNCA$_\infty$ for different N. Parameters: as in figure 10.

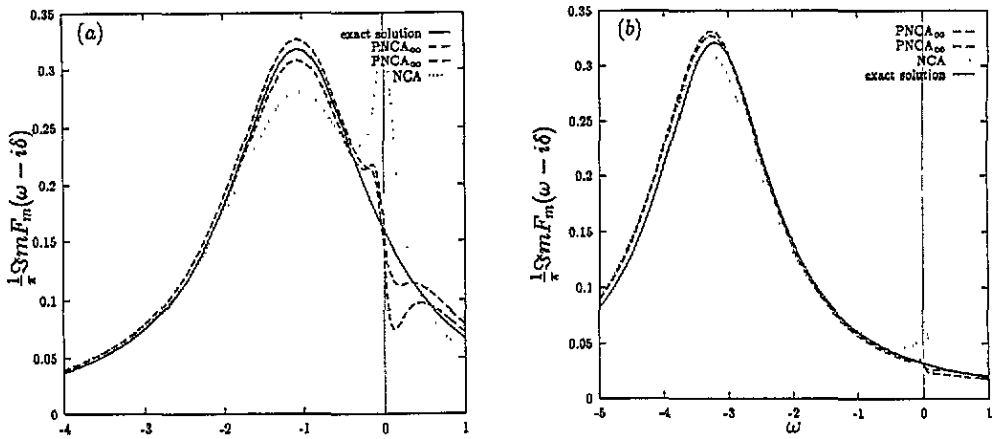

Figure 15. One-particle spectra in NCA and PNCA$_\infty$ compared with the *exact solution* for (a) $\epsilon_f = -\Delta$, $T = 1/15\Delta$ and (b) $\epsilon_f = -3\Delta$, $T = 1/60\Delta$. Parameter: $N = 1$.

reasonably fitted using a Lorentzian with a width of 0.95Δ. This reflects the fact that there is no blocking effect in this regime, whereas the local correlations still reduce the spectral weight to $\langle X_{00}\rangle + \langle X_{mm}\rangle = 0.87 < 1$.

7. Conclusion and outlook

We have demonstrated that our new PNCA$_\infty$ approximation to the Anderson model improves the low-energy properties in the Kondo regime quite remarkably, whereas the satisfactory behaviour of the old NCA approximation at higher energies is maintained. Vertex corrections do have in fact a large impact on the low-energy excitations: the position and height of the ASR for $N = 2$ is shifted towards the chemical potential as consistent with Friedel's sum rule. Also the magnetic susceptibility agrees surprisingly well with the Bethe *ansatz*

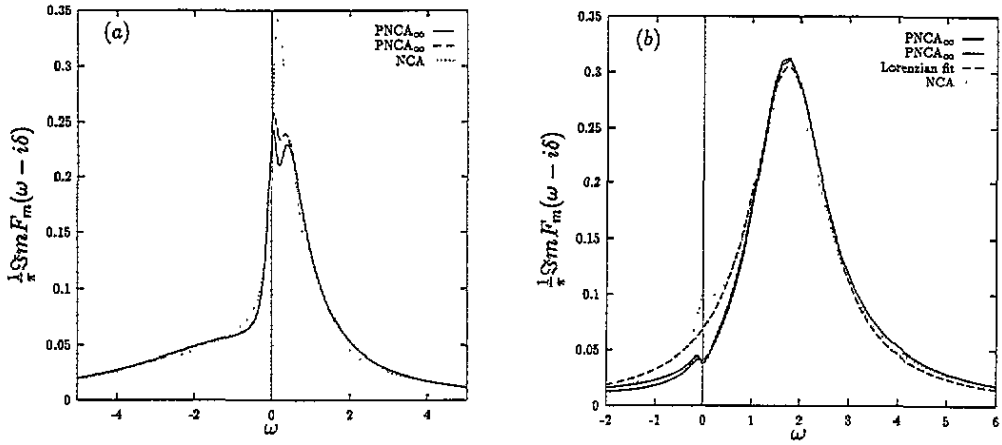

Figure 16. One-particle spectra in NCA and PNCA$_\infty$ for (a) $\epsilon_f = -\Delta$ and (b) $\epsilon_f = +\Delta$, the intermediate-valence regime. Parameters: $N = 2, T = \frac{1}{15}\Delta$.

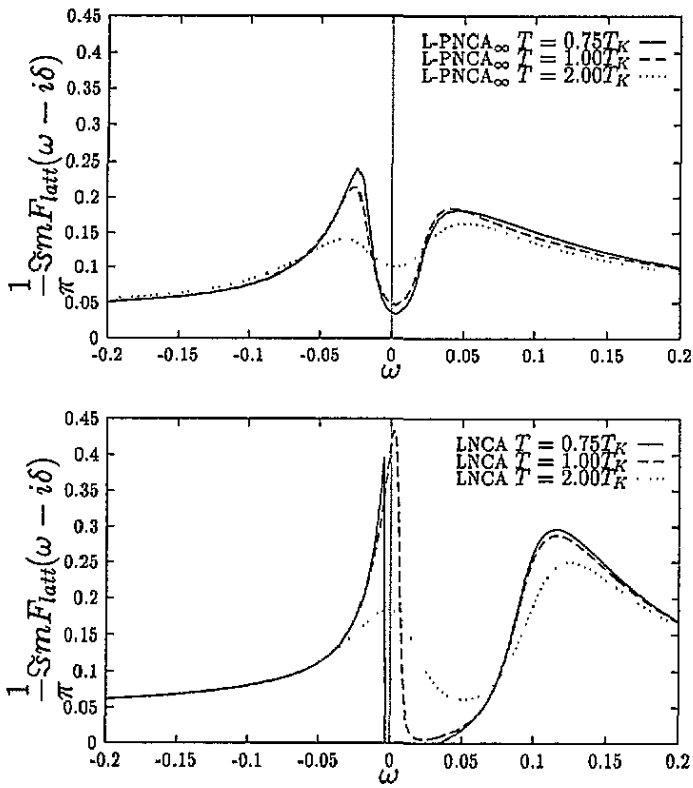

Figure 17. f-spectra of the periodic Anderson model in the vicinity of the chemical potential (a) in LPNCA$_\infty$ and (b) in LNCA for three temperatures $T = 0.75, 1.0, 2.0T_K$. Parameters $N = 2, \epsilon_f = -3\Delta, W = 10\Delta$.

results. We plan to apply this method also to the finite-U Anderson model and the extended Anderson model [9, 2], which includes a direct exchange interaction between

f and conduction electrons. The self-consistent set of equations has been derived already [4]. Our perturbational approach to the Anderson model has opened the prospect of studying the low-temperature properties of heavy-fermion systems in much more detail than before. Quite generally, the so-called LNCA scheme [8] can be applied, which provides a very successful perturbational treatment of the Anderson lattice. Within this theory based on a picture of independent effective sides plus quasiparticle interactions collective effects like superconducting or magnetic ground states can be calculated in a systematic way. In order to underline this perspective we present the temperature-dependent pseudogap formation in the f-spectrum of the Anderson lattice with $N = 2$ and $\epsilon_f = -3\Delta$ in figure 17. The temperatures are given in units of the corresponding impurity Kondo temperature which deviates moderately from the characteristic temperature of the lattice T^*. While the LNCA scheme combined with the local NCA is limited to temperatures larger than T_K due to violations of the local Fermi-liquid properties, the so-called LPNCA$_\infty$, which uses the PNCA$_\infty$ to solve the effective site, reaches much lower temperatures. Since now the ASR of the impurity is located only very slightly above the chemical potential in accordance with Friedel's sum rule, the pseudogap is formed around $\omega = 0$ in the LPNCA$_\infty$. In a forthcoming publication we will investigate the temperature-dependent quasiparticle band structure and the impact on the transport coefficients and optical conductivity in greater detail.

Acknowledgments

The author is very grateful to Professor N Grewe for many fruitful discussions on the subject of this work and careful reading of the manuscript. He would also like to acknowledge valuable conversations with Professor H Keiter, Professor J Keller, Dr Th Pruschke and Professor P Wölfle. This work has been performed within the partial requirements for a Dr. rer. nat at the Technische Hochschule Darmstadt.

References

[1] Anders F B, Grewe N and Lorek A 1991 *Z. Phys.* B **54** 293
[2] Anders F B, Qin Qi and Grewe N 1992 *J. Phys.: Condens. Matter* **4** 7229
[3] Anders F B and Grewe N 1994 *Europhys. Lett.* **26** 551
[4] Anders F B 1995 The Anderson models: an enhanced perturbational analysis *PhD Thesis* Technische Hochschule Darmstadt, unpublished
[5] Bickers N E 1987 *Rev. Mod. Phys.* **59** 845
Bickers N E, Cox D L and Wilkins J W 1987 *Phys. Rev.* B **36** 2036
[6] Costi T A, Schmitteckert P, Kroha J and Wölfle P 1994 *Phys. Rev. Lett.* **73** 1275
[7] Grewe N 1983 *Z. Phys.* B **52** 193; **53** 271
[8] Grewe N, Pruschke Th and Keiter H 1988 *Z. Phys.* B **71** 75
[9] Freytag P and Keller J 1991 *Z. Phys.* B **85** 87
[10] Hewson A C 1993 *The Kondo Problem to Heavy Fermions* (Cambridge: Cambridge University Press) ISBN 0-521-36382-9, and references therein
[11] Gruneberg J and Keiter H 1991 *Physica* B **171** 39
[12] Keiter H and Morandi G 1984 *Phys. Rep.* **109** 227
[13] Menge B and Müller-Hartmann E 1988 *Z. Phys.* B **73** 225
[14] Okiji A and Kawakami N 1984 *J. Appl. Phys.* **55** 1931
[15] Costi T A, Hewson A C and Zlatić V 1994 *J. Phys.: Condens. Matter* **6** 2519
[16] Pruschke Th and Grewe N 1989 *Z. Phys.* B **74** 439
[17] Rajan V T 1983 *Phys. Rev. Lett.* **51** 308